remote sensing

MDPI

Article

Study of Shale Gas Source Rock S-Wave Structure Characteristics via Dense Array Ambient Noise Tomography in Zhangjiakou, China

Si Chen [1], Zhanwu Lu [1,2,*], Haiyan Wang [1,2], Qingyu Wu [1], Wei Cai [1], Guowei Wu [1] and Guangwen Wang [1]

[1] Institute of Geology, Chinese Academy of Geological Sciences, Beijing 100037, China; chen_s@cags.ac.cn (S.C.); hyanwhy@126.com (H.W.); geoqyw@outlook.com (Q.W.); way.z.choy@gmail.com (W.C.); wuguowei19@mails.ucas.ac.cn (G.W.); wanggw@cags.ac.cn (G.W.)
[2] SinoProbe Laboratory, Ministry of Natural Resources, Beijing 100037, China
* Correspondence: luzhanwu@cags.ac.cn; Tel.: +86-13520374178

Abstract: Utilizing short-period dense seismic arrays, ambient noise tomography has proven effective in delineating continuous geological structures, a task critical for characterizing shale gas reservoir configurations. This study deployed 153 short-period seismic stations across the Xiahuayuan District in Zhangjiakou, a region with prospective shale gas deposits, to perform an ambient noise tomography survey. Through a meticulous process involving cross-correlation analysis, dispersion curve extraction, and subsequent inversion, a three-dimensional velocity structure model of the area was constructed. The model discerns subtle velocity changes within the 0–3 km depth interval, achieving a horizontal resolution of approximately 1.5 km in the 0–3 km stratum, thereby effectively delineating the shale reservoir structure. Integration of the velocity model with regional geological data facilitated a comprehensive interpretation and structural analysis of the prospective shale gas zone. Low-velocity anomalies observed within the velocity structure correspond to the spatial distribution of the Xiahuayuan Formation, likely attributable to the prevalent stratum of mudstone shale deposits within this formation. Employing a binary stratigraphic model, the study predicted shale content based on the velocity structure, with predictions exhibiting a moderate correlation (correlation coefficient of 0.58) with empirical data. This suggests the presented method as a viable rapid estimation technique for assessing the shale content of target strata.

Keywords: dense array; ambient noise tomography; shear wave velocity structure; shale gas reservoir

check for updates

Academic Editor: Fabio Rocca

Received: 18 October 2024
Revised: 12 December 2024
Accepted: 24 December 2024
Published: 7 January 2025

Citation: Chen, S.; Lu, Z.; Wang, H.; Wu, Q.; Cai, W.; Wu, G.; Wang, G. Study of Shale Gas Source Rock S-Wave Structure Characteristics via Dense Array Ambient Noise Tomography in Zhangjiakou, China. *Remote Sens.* **2025**, *17*, 183. https://doi.org/10.3390/rs17020183

Copyright: © 2025 by the authors. Licensee MDPI, Basel, Switzerland. This article is an open access article distributed under the terms and conditions of the Creative Commons Attribution (CC BY) license (https://creativecommons.org/licenses/by/4.0/).

1. Introduction

Shale gas, a natural gas confined within shale formations, is distinguished by its self-generation and self-storage capabilities, with a continuous accumulation pattern. The scale of shale gas reservoirs is predominantly governed by the extent of the shale reservoir distribution. In China, shale gas resources offer considerable economic potential due to their vast reserves, widespread occurrence, and the presence of multiple developed stratigraphic sequences [1–3]. However, the geological conditions for shale gas are intricate, encompassing marine, marine-terrestrial transitional, and terrestrial shales with multi-layered distribution, diverse origins, and complex subsequent modifications [4–6]. These factors compound the complexities of shale gas reservoir exploration and development.

Traditionally, delineating the distribution range of shale, a critical determinant of shale gas reserves, necessitates extensive active source seismic surveys or drilling data [5,7].

While three-dimensional active source seismic exploration can precisely outline the structural surface characteristics of shale reservoirs, and statistical analysis of drilling data can infer shale distribution, these methods are costly and laborious, impeding their use in preliminary exploration for rapid subsurface structural assessment. Thus, there is an imperative for an exploration technique that is operationally straightforward, economically viable, and capable of swiftly acquiring subsurface structural insights, as well as understanding geological formations and analyzing reservoir distribution characteristics.

Aki [8] pioneered research on passive source exploration methods, introducing the concept of microseismic detection for probing underground structures. Decades of evolution in this field culminated in Shapiro et al.'s [9] seminal paper on the background noise imaging method, signifying the maturation of this technique. Bensen et al. [10] subsequently consolidated the data processing workflow for background noise imaging, standardizing the procedure. The advent of ambient noise tomography (ANT) has emancipated surface wave-dominated exploration methods from the dependence on seismic sources, facilitating more agile underground structure detection. ANT, particularly when based on short-period dense arrays, can flexibly detect velocity structures at various depths, ranging from hundreds of meters to several kilometers [11–14], offering superior delineation of continuous regional structures.

Given that shale gas reservoirs are characterized by large, continuous distributions, the short-period dense array ANT is particularly suited for their detection. This study selects the Xiahuayuan District in Zhangjiakou, a shale gas prospective area, for short-period dense array ANT investigation. Deploying 153 nodal seismographs, the study collected continuous seismic noise records over a 15-day period. Employing cross-correlation calculations, dispersion curve extraction, and inversion, the research conducted imaging studies of the area. By integrating geological data from the region, the study provided a comprehensive interpretation of the velocity structure, analyzed the structural characteristics of the prospective area, and investigated the relationship between shale reservoir distribution and the velocity structure. This research contributes to the application of dense array methods in shale gas exploration and development.

2. Station Deployment and Geological Background

For the survey data acquisition phase of this study, Fairfield Zland nodal seismographs were utilized, with a total deployment of 153 units over a period of 15 days. These seismographs operated at a consistent sampling rate of 500 Hz, ensuring a high-quality dataset for analysis. The strategic positioning of the seismograph stations was informed by the geological characteristics and the stratigraphic development prevalent within the study area (Figure 1).

The layout of the seismograph array was tailored to the areas where the Jurassic strata are most prominently exposed. The design included a series of north-south oriented survey lines, which were complemented by a pattern of dispersed points in select areas. This approach was adopted to achieve a uniform distribution of stations across the region, thereby enhancing the spatial resolution of the subsurface velocity structure model. The resultant detection array spanned an east-west length of approximately 25 km and a north-south width of about 15 km, as illustrated in Figure 2. This configuration was instrumental in capturing the intricate geological attributes of the region, which are essential for the accurate assessment of the shale gas reservoir potential.

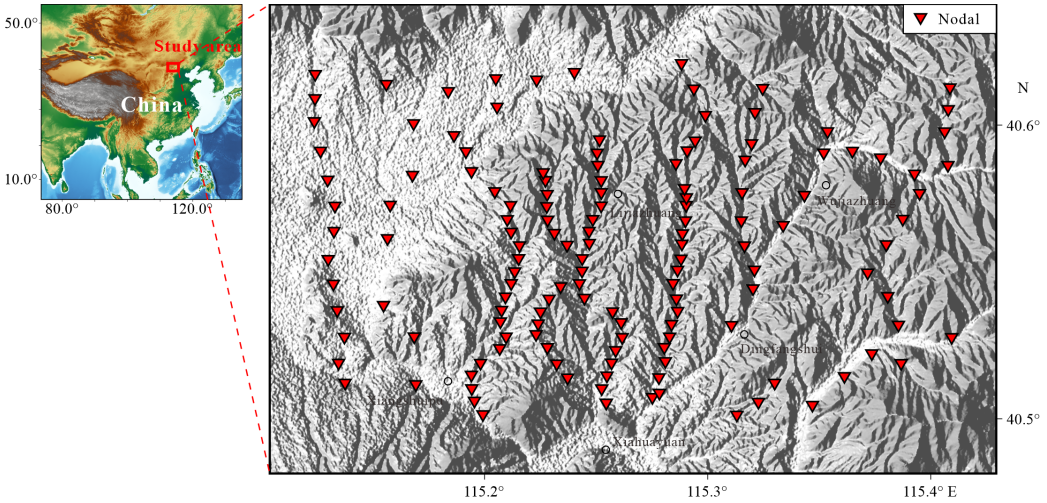


Figure 1. Location of nodal seismographs station deployment in the research area.

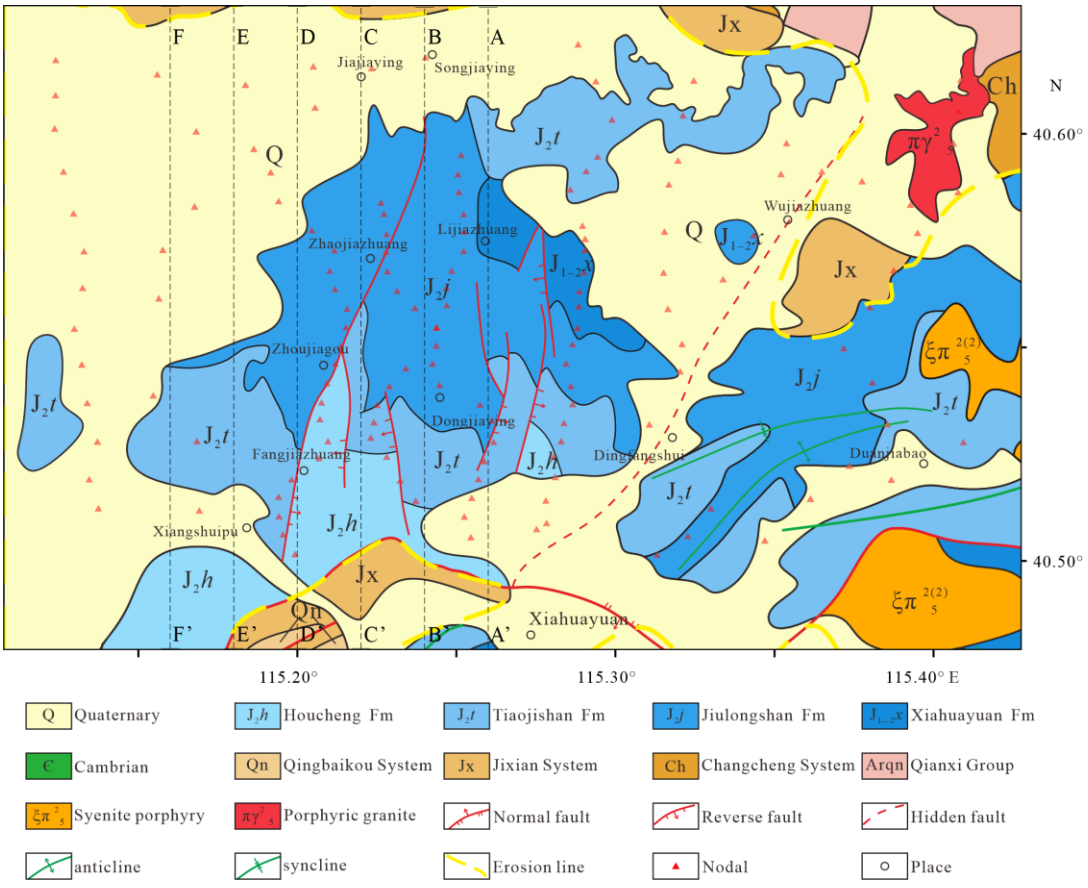


Figure 2. Regional geological features and station locations (geological map provided by the Hebei Coalfield Geological Exploration Institute).

The study area, situated within the Xiahuayuan District of Zhangjiakou City in Hebei Province, is underlain by a sequence of strata predominantly belonging to the Jurassic System, succeeded by the Jixian System and the Qingbaikou System. The Jurassic strata are predominantly characterized by a monoclinal structure that dips towards the southwest, with the depth of burial increasing progressively from the northern to the southern extents of the region (Figure 2).

Within this context, the Xiahuayuan Formation ($J_{1-2}x$) (Figure 3) of the Jurassic System emerges as the principal shale gas reservoir and a significant coal-bearing stratum [15–17].

This formation is predominantly composed of dark mud shale and sandstone, often exhibiting interbedded sand-mudstone structures, and encompasses multiple layers of coal seams with exploitable potential. Additionally, the Qingbaikou System's Xiamaling Formation (Qn*x*), which underlies the Xiahuayuan Formation, is recognized as another significant shale gas reservoir within the region [18,19]. It is predominantly composed of thin black shale layers and is in non-conformable contact with the overlying Xiahuayuan Formation.

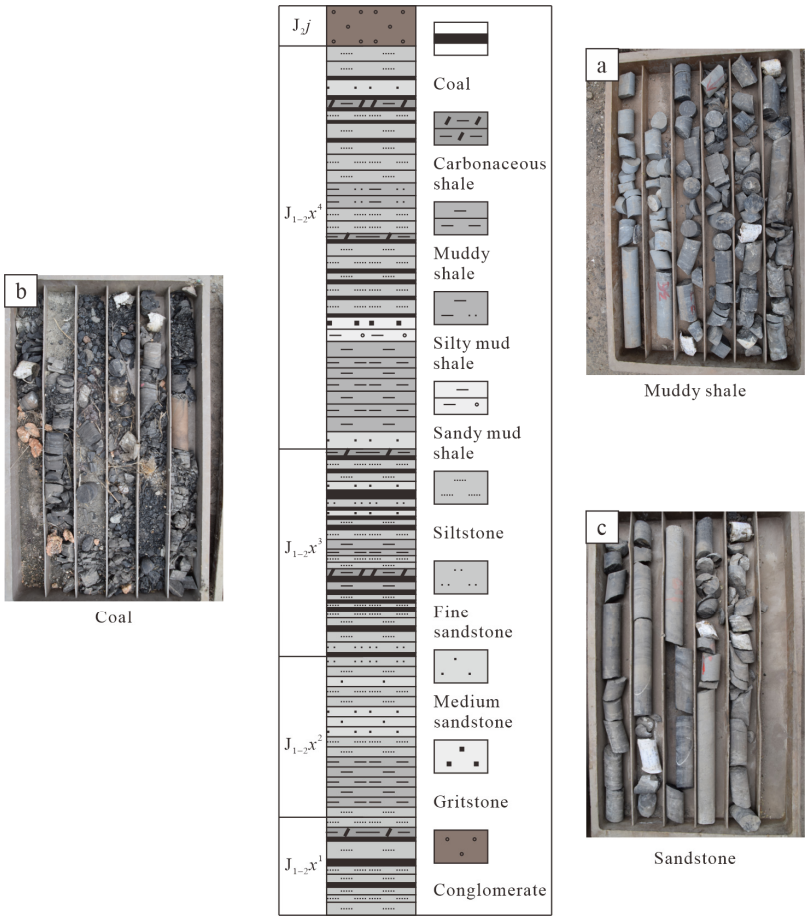


Figure 3. Stratigraphic column of the Xiahuayuan Formation. the (**a**,**b**) image is the mudstone shale and coal of the Xiahuayuan Formation. The rocks mainly exhibit thin layers and are relatively fragmented. (**c**) mainly shows the sandstone layer in the lower part of the Xiahuayuan Formation with intact structure. The data are provided by the Hebei Coalfield Geological Exploration Institute.

The study area also includes other Jurassic stratigraphic units such as the Houcheng Formation (J_2h), the Tiaojishan Formation (J_2t), and the Jiulongshan Formation (J_2j). The deployment of seismic stations across this geologically diverse region was strategically designed to capture the intricate subsurface architecture, which is critical for the accurate assessment of shale gas potential.

3. Method

3.1. Cross-Correlation Calculations

The initial phase of preparing for cross-correlation calculations conformed to the comprehensive workflow delineated by Bensen et al. [10]. The preprocessing of single station data included three key steps: (1) Only the Z-component seismic records were utilized and resampled to 20 Hz, and detrending was performed. These records were then segmented into 24 h lengths to facilitate cross-correlation calculations. Considering the seismographs were deployed in hilly regions with minimal human interference, a linear

stacking method was employed for cross-correlation analysis, thus maintaining the integrity of the waveforms. (2) Time-domain normalization was applied, using running-absolute-mean normalization, which adjusts the waveform by a moving average of its absolute value, reducing the impact of earthquakes, instrumental inconsistencies, and non-stationary noise sources near stations on cross-correlations. (3) Spectral whitening was implemented to address broad imbalances in single station spectra and to expand the bandwidth of the ambient noise signal, thereby achieving a more continuous dispersion curve.

Both theoretical insights and practical applications have demonstrated that the empirical Green's function (EGF) between station pairs can be derived from the time derivative of the noise cross-correlation function, which can be succinctly expressed as follows [14,20]:

$$\frac{dC_{AB}(t)}{dt} = -\hat{G}_{AB}(t) + \hat{G}_{BA}(-t) \approx -G_{AB}(t) + G_{BA}(-t) \quad (1)$$

In the formula, $C_{AB}(t)$, $\hat{G}_{AB}(t)$ and $G_{AB}(t)$ represent the ambient noise cross-correlation function, the empirical Green's function (EGF), and the real Green's function between two station pairs A and B, respectively.

Utilizing the aforementioned formula, both a positive and a negative branch can be derived from the cross-correlation calculation of any two time series. These branches are designated as the causal signal and the acausal signal, respectively, representing the two opposing directions of wave propagation. In scenarios where the noise source is uniformly distributed, the signals captured by the two branches are expected to exhibit symmetry. However, in actual observations, asymmetry between the positive and negative branches is frequently observed, attributed to the uneven distribution of noise sources. Figure 4 illustrates the cross-correlation function between station 6153 and all other stations, highlighting the emergence of a distinct Rayleigh surface wave within the 1–6 s band. The surface wave remains discernible even at a distance of 25 km, indicative of a high signal-to-noise ratio. The amplitude on the positive lag time is marginally more pronounced than that on the negative lag time, potentially due to the inhomogeneous distribution of noise sources.

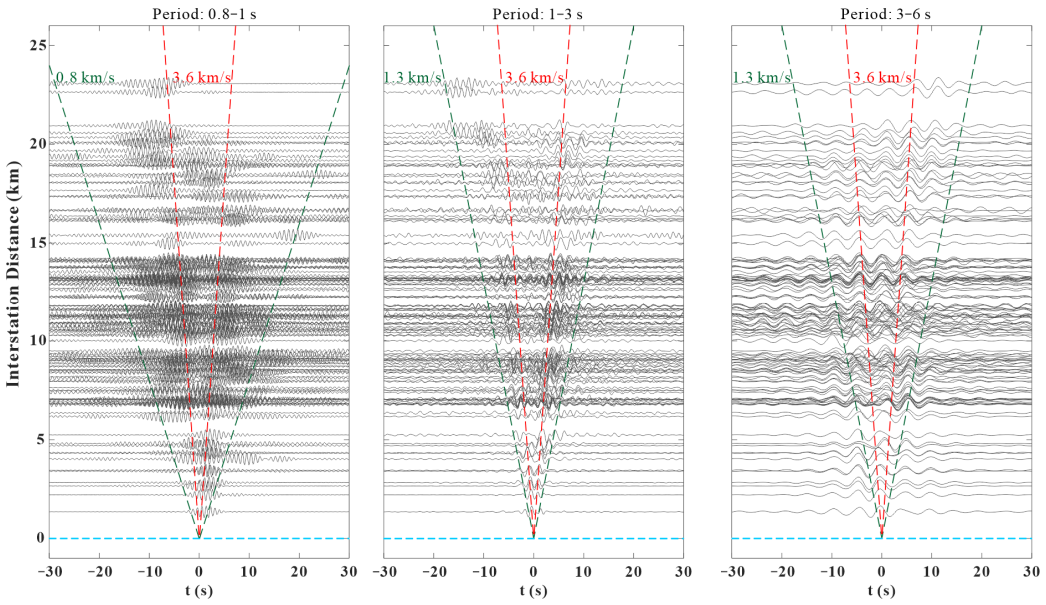


Figure 4. Station 6153 cross-correlates results with other stations. The image illustrates the characteristics of surface waves in the array with various bandpass filters, and these characteristics are effectively captured within the filtering parameters of 0.8–6 s.

Post-processing of the cross-correlation results involved arranging the outcomes by distance to discern the surface wave characteristics. A series of band-pass filtering tests were conducted on the cross-correlation data. Distinct surface wave signals were identified within the filter intervals of 0.8–1.0 s, 1.0–3.0 s, and 3.0–6.0 s. Specifically, when applying a band-pass filter from 0.8 to 1.0 s, the surface wave velocities were predominantly observed in the range of 0.8–3.6 km/s, with continuous wave signals up to a distance of 0–15 km. With a filter range of 1.0 to 3.0 s, the velocities were mainly between 1.3–3.6 km/s, exhibiting continuous signals up to 0–20 km. For the 3.0–6.0 s filter interval, the surface wave signals remained clear and continuous at distances beyond 20 km. Collectively, these observations suggest that within the period range of 0.8–6.0 s, the surface wave signals in the study area exhibit robust strength and continuity (Figure 4).

3.2. Dispersion Extract Curve

In this study, the retrieval of group velocity dispersion curves was accomplished through the time-frequency analysis method known as EGFAnalysisTimeFreq (EGFA), initially introduced by Yao et al. [21,22]. This technique employs a series of filtering strategies, as detailed by Dziewonski et al. [23], to extract the fundamental mode surface wave group velocity dispersion images for a given station pair. The dispersion curves were then extracted by analyzing the energy distribution characteristics within these images (Figure 5). The EGFA method was employed to accurately derive the dispersion curves. Despite challenges in pinpointing the precise interval of the phase velocity diagram due to 2π disturbances, the group velocity image's energy concentration was readily detectable, exhibiting superior continuity across all periods and accurately reflecting the changes in Rayleigh's subsurface group velocity. The study primarily relied on group velocity for the extraction of dispersion curves.

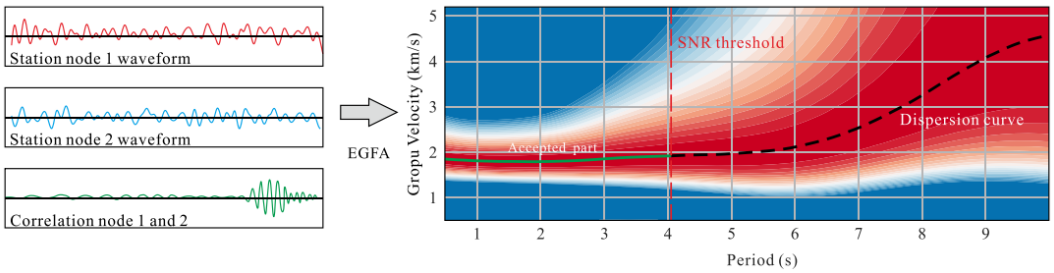


Figure 5. Dispersion curve extraction process schematic diagram.

To enhance the precision of dispersion measurements, the signal-to-noise ratio (SNR) of the cross-correlated waveform data was initially calculated. A group velocity window, defined by (*Vmin*, *Vmax*), was employed, with the arrival time window of the surface wave determined by the formulae $t1 = \triangle/Vmax$ and $t2 = \triangle/Vmin$, where $\triangle$ represents the inter-station distance. The signal is identified as the surface wave within the arrival time window, while noise is considered to be outside this signal window. Building on previous research in this region, the group velocity window was fine-tuned, and cross-correlation data with an SNR exceeding 1 was selected, ensuring that only high-quality waveform data were retained.

Dispersion curves were manually measured within a period range of 1–6 s, with a sampling period of 0.1 s. To ensure the accuracy and reliability of the measurements, several criteria were applied: adherence to the far-field approximation (with station distances exceeding twice the wavelength), maintenance of a signal-to-noise ratio greater than 1, continuity of the dispersion curve, and similarity of dispersion curves between adjacent station pairs. Furthermore, in line with previous studies in this area [24,25], the group

velocity values of the dispersion curves were confined to a range of 0.5–3.6 km/s, with the average velocity change rate limited to within 0.3 km/s for periods from 0 to 6 s. After this rigorous selection process, a dataset comprising 4200 high-quality dispersion curves was compiled (Figure 6).

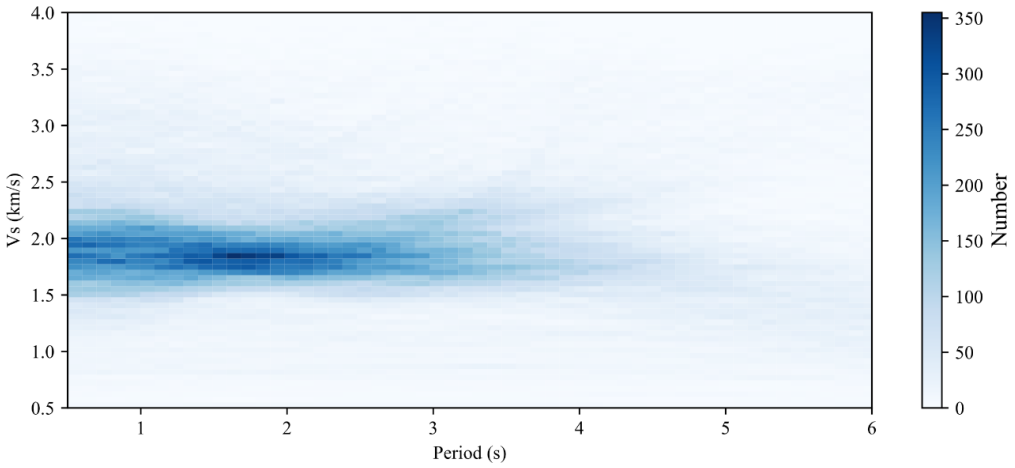


Figure 6. Characteristics of the overall distribution of the dispersion curve. The features of the dispersion curve collection are illustrated via a 2D histogram. Between 0 and 3 s, the dispersion curve features are more concentrated, whereas after 3 s, the dispersion curves become more dispersed. This suggests that the shallow subsurface structures are straightforward, whereas the deep subsurface structures are complex.

3.3. Depth Inversion

(1) Inversion method

Direct S-wave velocity tomography was conducted utilizing the surface wave dispersion inversion method proposed by Fang et al. [26], bypassing the traditional two-step inversion's intermediate phase or group velocity inversion [27]. The fast marching method was employed for computing surface wave travel times and ray paths, circumventing the great-circle propagation assumption, which is unsuitable for complex media. The S-wave velocity inversion objective function is given by [26]:

$$\Phi(\mathrm{m}) = \|d - Gm\|_2^2 + \lambda \|Lm\|_2^2 \quad (2)$$

Here, d represents the residual vector of observed and theoretical travel times, G is the data sensitivity matrix, m is the model parameter vector, λ is the weight parameter that balances data fitting and model regularization, and L is the smoothness constraint for the model, often the first- or second-order spatial derivative operator [28]. The S-wave velocity distribution is derived by minimizing this objective function. An increased weight parameter λ results in smoother inversion results with lower resolution, and vice versa. A properly selected weight ensures reasonable velocity changes at each iteration. To determine the optimal weight λ, balancing data residual and model regularization, L-curve analysis is commonly employed to identify the weight corresponding to the inflection point on the L-curve, indicating the best weight.

(2) Initial velocity model

For the initial velocity model and inversion, a sensible 1D initial velocity model can be established based on available dispersion data. The calculated dispersion curve can be transformed into an S-wave velocity model (Depth-Vs) using empirical formulas, taking the shear velocity as 1.1 times the surface waves velocity and the depth as one-third of the corresponding wavelength [14,29]. Considering the longest period of the dispersion curve and inversion requirements, the model's maximum depth was set at 5 km. In light

of previous studies in this area [24,25] and inversion tests, the surface and 5 km depth vs. were set to 0.5 km/s and 3.6 km/s, respectively. The velocity gradient is 0.6 s^{-1}.

Finally, the inversion model, which was structured on a layered basis, featured a planar grid configuration of 44 × 22. The grid dimensions equated to an approximate length of 0.008° × 0.008°, translating to roughly 800 m. The model encompassed a depth grid comprising 17 nodes. The interval between layers was set at 200 m in the upper section (ranging from 0 to 2000 m) and increased to 400 m in the deeper stratum (from 2000 to 4800 m). Following 10 iterations of computational analysis, the travel time residual, denoted as the root mean square (RMS) of the residual, showed a significant reduction from an initial value of 2.5 to a final value of 0.1. The parameters converged towards zero, signifying that the model inversion had achieved convergence and stability after the 10th iteration (Figure 7).

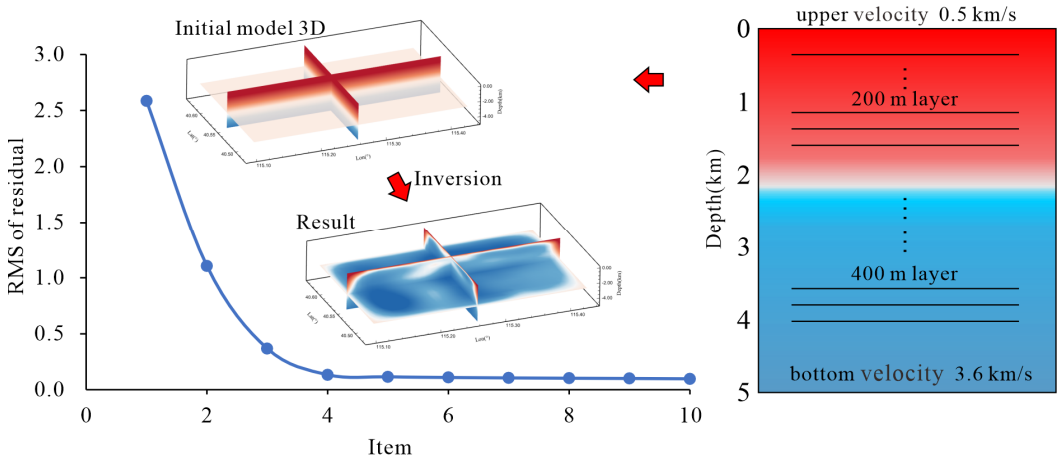


Figure 7. The number of iterations and the trend of parameter changes.

4. Results

4.1. Reliability Analysis

(1) Sensitivity Kernel Test

The sensitivity kernel is a critical parameter that quantifies the responsiveness of subsurface medium parameters to perturbations in surface wave travel times. For a surface wave of a specified period, the sensitivity kernel's profile typically manifests a peak value within a particular depth interval. The depth corresponding to this peak value denotes the level at which the medium parameters are most sensitive to the surface wave for the given period. To ascertain the depth sensitivity characteristics of the model, this study executed a sensitivity depth test on the derived model using the CPS330 suite of tools, as referenced by Herrmann [30]. To delineate the three-dimensional (3D) sensitivity attributes of the model, a depth sensitivity kernel test was conducted on every node within the model. The outcomes of these tests were subsequently superimposed and normalized to encapsulate the aggregate sensitivity kernel traits of the 3D model. The test encompassed periods from 0.5 to 6.0 s. At a period of 0.5 s, the apex of the sensitivity kernel corresponds to a depth of 0.5 km, and at a period of 5 s, the peak is observed to be proximal to 5 km, with the sensitivity kernel's maximum value demonstrating essentially a linear progression. The sensitivity kernel test corroborates that dispersion curves within the period range of 0.5 to 6.0 s are capable of effectively delineating the subsurface structure down to a depth of 5 km (Figure 8).

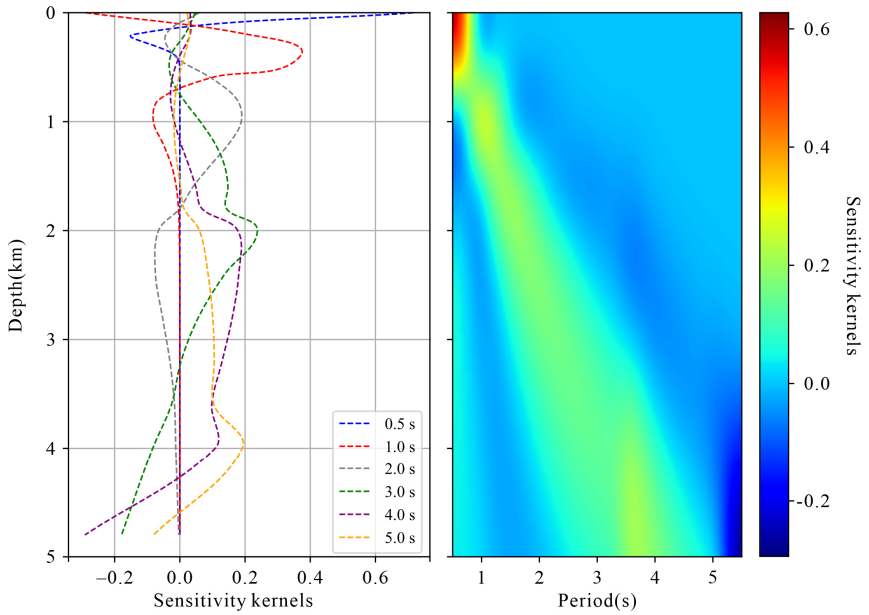


Figure 8. Average sensitivity kernel testing. The figure illustrates that the velocity structure model responds well to depths of 0–5 km.

(2) Checkerboard Test

The checkerboard test is a widely accepted method for qualitatively evaluating the horizontal resolution of an inversion result model. This technique involves comparing a theoretical model with its inversion solution to qualitatively determine the resolution length, thereby assessing the model's resolving power. The principle is straightforward: if the model can accurately replicate the anomalies from a known theoretical model, the resolution is deemed to be half the size of the anomalies' grid dimensions. This approach is a standard in the literature for resolution testing within the field of noise imaging research [12,31,32].

In the context of this study, a checkerboard test was performed on the inversion model to ascertain its capacity to resolve anomalies. A square anomaly measuring 3.0 km by 3.0 km was introduced, and the checkerboard test was utilized to replicate this anomaly. The velocity perturbation was ±5% with respect to the initial model. The reproduction results demonstrate that within the depth interval of 0 to 2.8 km, the anomalies are well recovered. This outcome suggests that the model is adept at resolving anomalies with a scale of 1.5 km at depths shallower than 2.8 km. Consequently, the ensuing discussion will concentrate on the regions where the anomalies are effectively reproduced at these shallow depths (Figure 9).

4.2. Velocity Structure

The shear wave velocity values derived from the inversion model range from 0.6 to 3.4 km/s, with horizontal slices representing depths from 0 to 3.0 km (Figure 10). At a depth of 0.5 km, some distinct low-velocity anomalies are observed, with portions of this anomaly distributed along the northeastern periphery of the study area, while another part is predominantly situated in the central region of the slice.

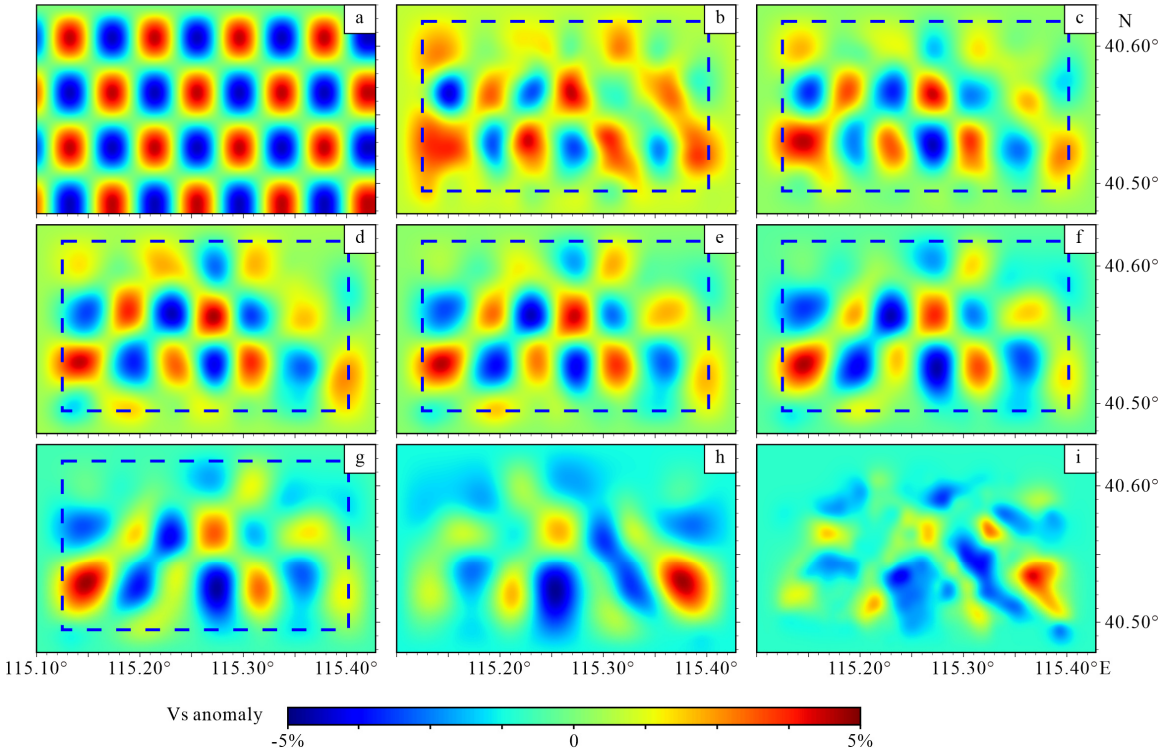


Figure 9. Checkerboard test results at different depths. The dense array data were tested respectively with synthetic 5% Gaussian random noise. The figure reflects the ability of the velocity structure model to resolve anomalies with a scale of 1.5 km. The (**a**) represents the checkerboard pattern model, while (**b**–**i**) correspond to depths of 0.8 km, 1.2 km, 1.6 km, 2.0 km, 2.4 km, 2.8 km, 3.6 km, and 4.8 km, respectively. The dashed box is the area with the better recovery effect. Based on the results, it is evident that the recovery effect is more pronounced within the range of 1–3 km.

Upon examining the 1.0 km depth slice, the low-velocity anomalies previously noted in the northeastern direction have dissipated, and those in the central region have progressively shifted southward, transitioning from an east-west orientation to a north-south alignment. Within the depth interval of 1.0 to 2.5 km, the low-velocity anomalies exhibit relative stability and gradually diminish as they extend deeper to 2.5 km.

At a depth of 0.5 km, the low-velocity structure broadly correlates with the outcrop distribution of the Xiahuayuan Formation. This formation, prevalent within the study area, is rich in shale and coal layers, which are more conducive to generating low-velocity anomalies. It is hypothesized that these anomalies predominantly delineate the distribution scope of the Xiahuayuan Formation. Given that the burial depth of the Xiahuayuan Formation increases progressively from north to south across the region, the observed distribution characteristics of the low-velocity structure may be attributed to this formation.

Furthermore, a pronounced low-velocity structure is identified on the northwestern flank of the study area. However, the downward continuation of this anomaly is constrained, which, coupled with the substantial Quaternary deposits in this region, suggests that this anomaly may be associated with the superficial Quaternary sediments.

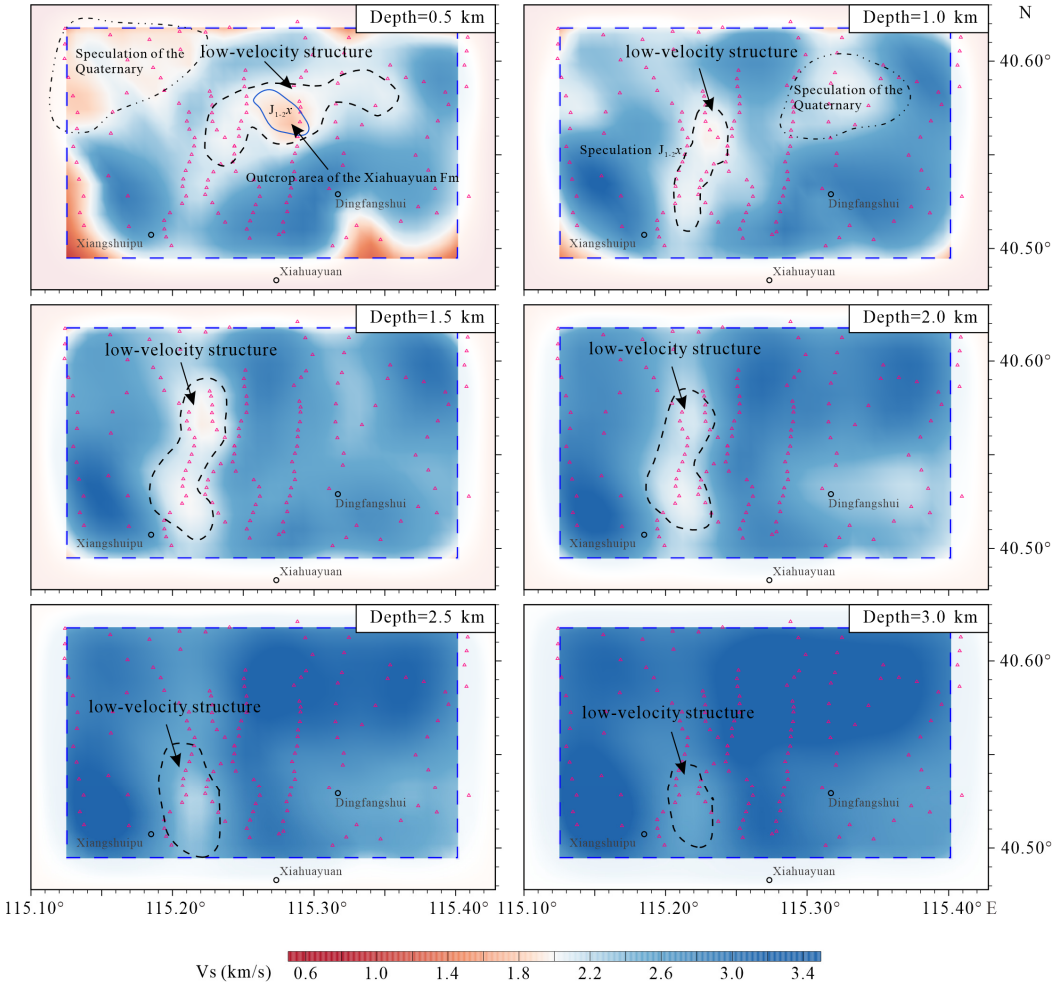


Figure 10. Depth slice features of shear wave velocity structure. The image demonstrates the characteristics of low-velocity structures. In the strata at a depth of 0–3 km, the occurrence of low-velocity structures closely aligns with the distribution of the Xiahuayuan Formation. Triangles represent stations.

5. Discussion

5.1. Underground Structure

The characteristics of the velocity structure suggest a correlation between the distribution of low-velocity anomalies and the stratigraphic distribution of the Xiahuayuan Formation, which is enriched with shale layers and is likely the primary cause of these anomalies. To further investigate the relationship between the velocity structure and the thickness of shale within the Xiahuayuan Formation, this study collated data from 31 drilling sites across the study area. The analysis synthesizes the burial characteristics and the shale thickness profile of the Xiahuayuan Formation to elucidate the velocity structure.

The drilling data reveal that the burial depth of the Xiahuayuan Formation increases progressively from north to south, with the stratum thickening accordingly. The burial depth can reach 1000–1200 m in the vicinity of Zhoujiazhuang and Qijiazhuang and extends up to 1500 m at Fangjiazhuang. The effective shale of the Xiahuayuan Formation is predominantly found in the regions of Lijiazhuang, Xiangshuipu, and Xiahuayuan, with shale bed thicknesses ranging from 50 to 300 m. Notably, the thickest shale deposits, reaching up to 300 m, are observed near Zhoujiazhuang and Fangjiazhuang (Figure 11).

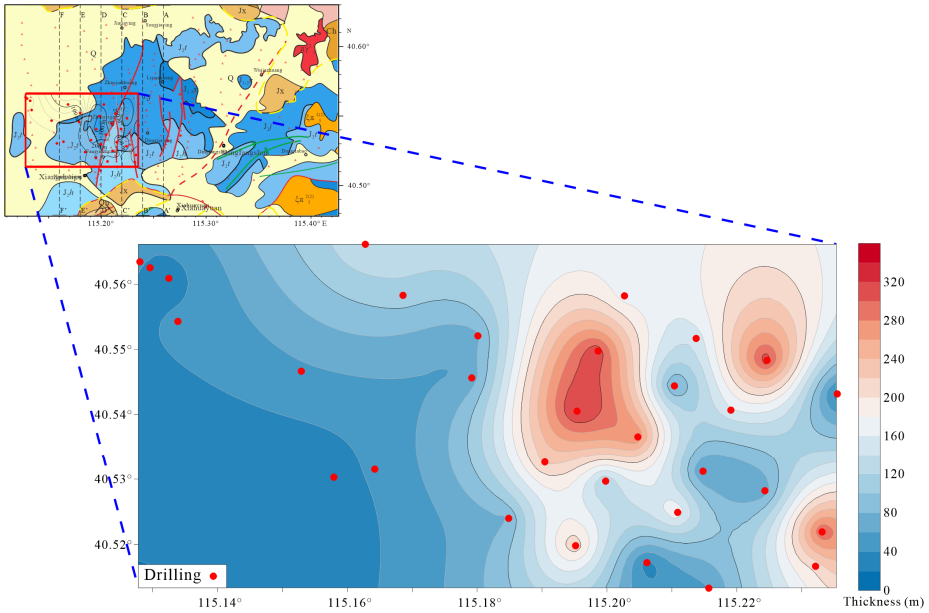


Figure 11. Mudstone shale contours of Xiahuayuan formation. This study compiled contour features of the thickness of the Xiahuayuan Formation from all the drilling wells. Note that some wells did not penetrate the Xiahuayuan Formation; thus, the thicknesses represent only those revealed by the drilling.

Six north-south oriented velocity structure profiles were extracted for a detailed analysis of the subsurface architecture (Figure 12). Profile AA′ traverses the outcropping layers of the Xiahuayuan Formation. The profile illustrates that the low-velocity structure emerging at the surface continues to extend downward, with a belt-like low-velocity structure evident beneath, deepening progressively from north to south, reaching a depth of 1.5 km in the southern extent. This trend aligns with the burial characteristics of the Xiahuayuan Formation within the study area. Given the prevalence of shale and other low-velocity layers in the Xiahuayuan Formation, and considering the drilling depth data, it is postulated that this low-velocity structure is indicative of the stratigraphic extension of the Xiahuayuan Formation. In profile BB′, a more extensive area of low-velocity anomalies is observed at a deeper level near Lijiazhuang. Since the underlying Xiamaling Formation also contains a significant amount of shale, it is hypothesized that these anomalies may be attributed to the shale within the Xiamaling Formation. In profile CC′ and DD′, the low-velocity anomalies are even more pronounced, and drilling data indicate that the shale thickness in this region can reach 300 m, marking the epicenter of shale deposition. This finding further corroborates the notion that shale is a primary contributor to the development of low-velocity structures. Within this profile, a substantial area of low-velocity structures is also observed within a depth range of 1 km below the Xiahuayuan Formation, which is conjectured to be influenced by the underlying Xiamaling Formation. In profile EE′ and FF′, the extent of low-velocity anomalies is diminished, predominantly manifesting below the Xiahuayuan Formation, leading to the speculation that the shale content of the underlying Xiamaling Formation may be relatively higher. Concurrently, drilling data also indicate a sharp reduction in shale thickness in the area west of Zhoujiazhuang, where the thickness decreases from 300 m to 50 m.

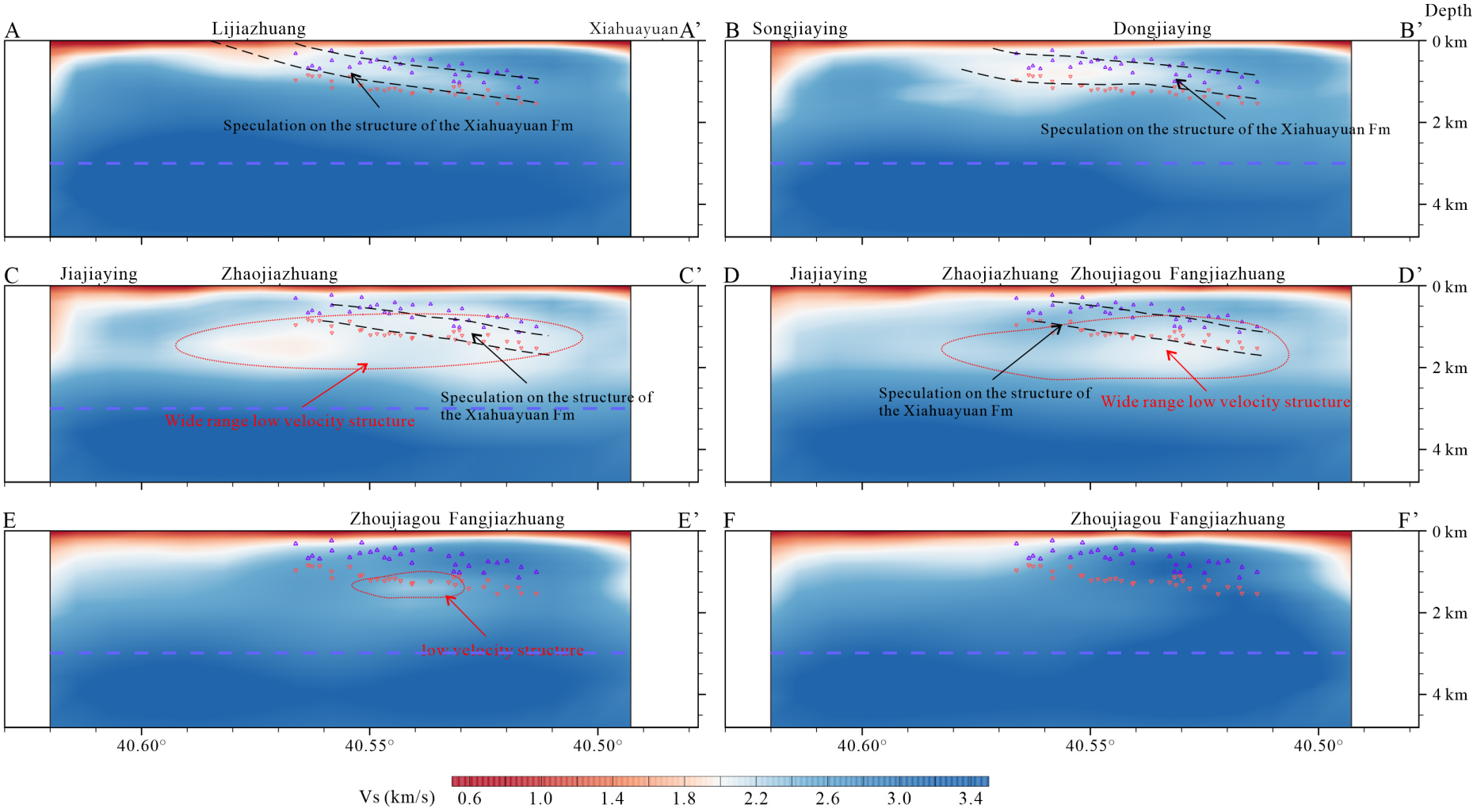


Figure 12. City structure vertical slice. The blue and red triangle represents the top and bottom boundary of the Xiahuayuan Formation by well drilling. In the absence of drilling data within the (**AA′**,**BB′**) profiles, it is inferred that the low-velocity structure is attributable to the muddy shale of the Xiahuayuan Formation. In the (**CC′**,**DD′**) profiles, the deeper low-velocity structures are more likely to be caused by the muddy shale of the Xiamaling Formation. Please refer to Figure 1 for the (**AA′**–**FF′**) position.

The overarching velocity structure characteristics suggest that the Xiahuayuan Formation predominantly exhibits a monoclinal structure dipping towards the south, with the shale within the formation consistently exhibiting low velocities. It is inferred that the primary development zone of the shale is in close proximity to Zhaojiazhuang, Zhoujiazhuang, and Fangjiazhuang. The velocity structure is reflective of the stratigraphic architecture and is congruent with the actual drilling data. Consequently, it is deduced that the noise imaging method can effectively delineate the reservoir structural characteristics within the prospective shale gas area.

5.2. Estimation of Source Rock Thickness

(1) Thickness estimation method

The interlayer velocity difference method, a staple in reflection seismic exploration, encompasses intricate procedures such as time-depth conversion, velocity spectrum construction, and compaction curve drawing for formation prediction, often necessitating the support of logging data [33–35]. However, surface wave inversion offers a direct means of acquiring subsurface velocity data, simplifying the analysis of depth–velocity relationships within strata. For formations with a relatively uncomplicated lithological composition, a binary stratigraphic model can predict stratigraphic structures, such as the intermingled structure of sandstone and mudstone. Employing an equivalent model allows complex actual strata to be treated as equivalent simple strata, thus predicting the lithology within them (Figure 13). In the case of the strata examined in this study, the rock composition is intricate, comprising not only sandstone and mudstone shale but also coal seams. To streamline the analysis, the strata are broadly categorized into two groups: high-velocity rocks primarily consisting of siltstone and fine sandstone, and low-velocity rock layers primarily consisting of argillaceous sandstone, mudstone shale, and coal rock.

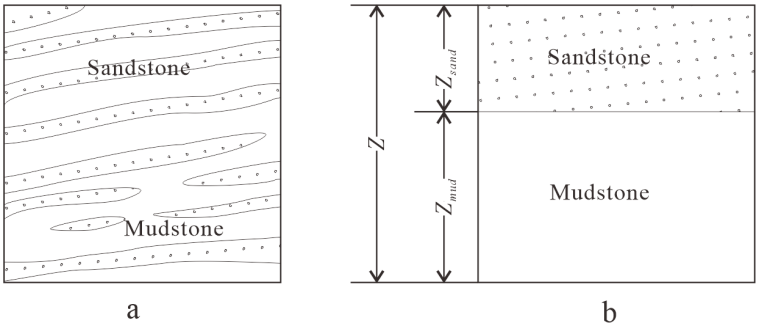


Figure 13. Binary stratigraphic model: (**a**) actual strata; (**b**) equivalent model.

Obtaining the thickness parameter of shale is key to evaluating shale gas resources. Accurate estimation requires a substantial amount of drilling data and experimental data, which can be difficult to obtain in areas with lower levels of shale gas exploration. Seismic wave velocity can reflect the physical properties of the medium through which it travels, thus allowing the prediction of lithology by analyzing the distribution characteristics of wave velocities. In practice, due to significant variations in lithology, the changes in seismic wave velocity within rocks are much more complex. Accurately predicting the lithology of strata requires knowledge of the seismic wave velocity characteristics for each type of rock. To facilitate the discussion of lithological characteristics, the lithology prediction model can be simplified by dividing the strata into two types for analysis: one with a higher seismic wave velocity, referred to as rock type A, and the other with a lower seismic wave velocity,

referred to as rock type B. The velocity variation for a binary stratum can be represented in the following form (Formulae (3)):

$$\frac{1}{V} = \frac{P_B}{V_B} + \frac{P_A}{V_A} \tag{3}$$

Here, P_A and P_B represent the proportions of rock types A and B, respectively, V_A and V_B are the seismic wave velocities for rock types A and B, respectively, and the sum $P_A + P_B$ equals 1, assuming the stratum is composed solely of these two rock types.

(2) Analysis of the variation of velocity with depth

Given that seismic wave velocities vary with burial depth, acquiring velocity values at different depths is crucial for predicting lithological distribution within the binary velocity prediction model. In the absence of drilling data, velocity spectra can be utilized to estimate the distribution of velocity values. By plotting the depth–velocity correspondence points from the inverted velocity structure of the target area onto the velocity distribution (Figure 14), the distribution of lithology can be inferred. The right envelope line of the scatter distribution area, representing higher velocities, is attributed to rock A, while the left envelope line, representing lower velocities, is attributed to rock B. Fitting these curves allows for the derivation of equations describing the velocity variation with depth for both rocks, thereby enabling the estimation of the shear wave velocities of rocks A and B at various depths.

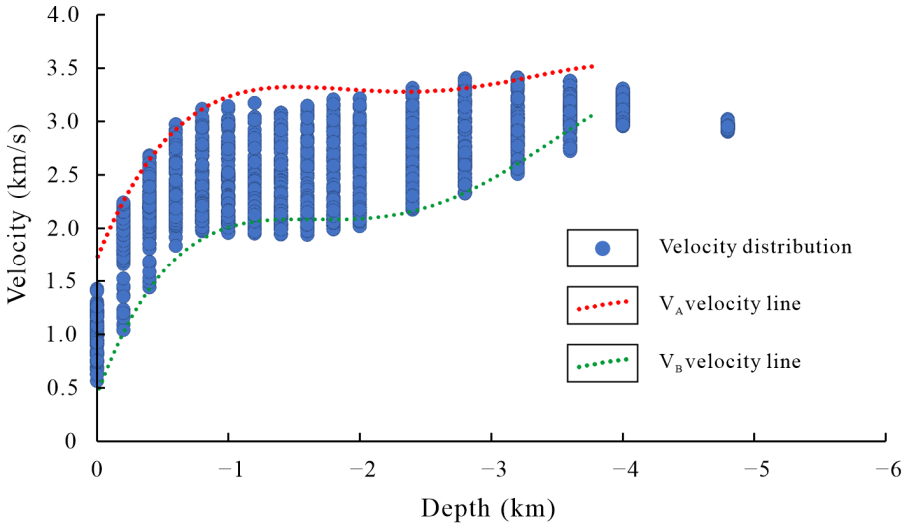


Figure 14. Velocity distribution with depth characteristics of the drilling area.

Integrating the above results, the calculation for the content of rock B in the target layer can be expressed in the following form (Formulae (4)):

$$\begin{cases} P_B = n^{-1} \cdot \sum_{i=1}^{n} \dfrac{V^{-1} - V_A(H_i)^{-1}}{V_B(H_i)^{-1} - V_A(H_i)^{-1}} \\ V_A(H) = -0.0547H^4 - 0.5729H^3 - 2.0785H^2 - 3.1147H + 1.6095 \\ V_B(H) = -0.0615H^4 - 0.6281H^3 - 2.105H^2 - 2.9112H + 0.589 \end{cases} \tag{4}$$

Here, P_B denotes the proportion of rock B in the target layer, H indicates depth, n is the number of equal divisions made for the target stratum, H_i corresponds to the midpoint depth of a division, $V_A(H_i)$ signifies the velocity value of rock A at depth H_i, and $V_B(H_i)$ represents the velocity value of rock B at the same depth H_i.

(3) Predicting lithological distribution

The results indicate that areas with higher rock B content are located on the eastern side of the region, while areas with lower content are on the western side (Figure 15). When compared with the shale content of the Xiahuayuan Formation from drilling data, the distribution characteristics are relatively consistent with the predicted content of rock B. However, the low-velocity rock content predicted by this method is significantly higher than the shale content in the drilling statistical data, which may be attributed to several factors: The Xiahuayuan Formation contains multiple thin layers of shale, potentially forming more loosely structured intervals that manifest as additional low-velocity layers, leading to a higher predicted result from the seismic wave velocity analysis. Other low-velocity rocks, such as coal seams, fine-grained sandstones, and silty fine sandstones, may also contribute to the predicted results.

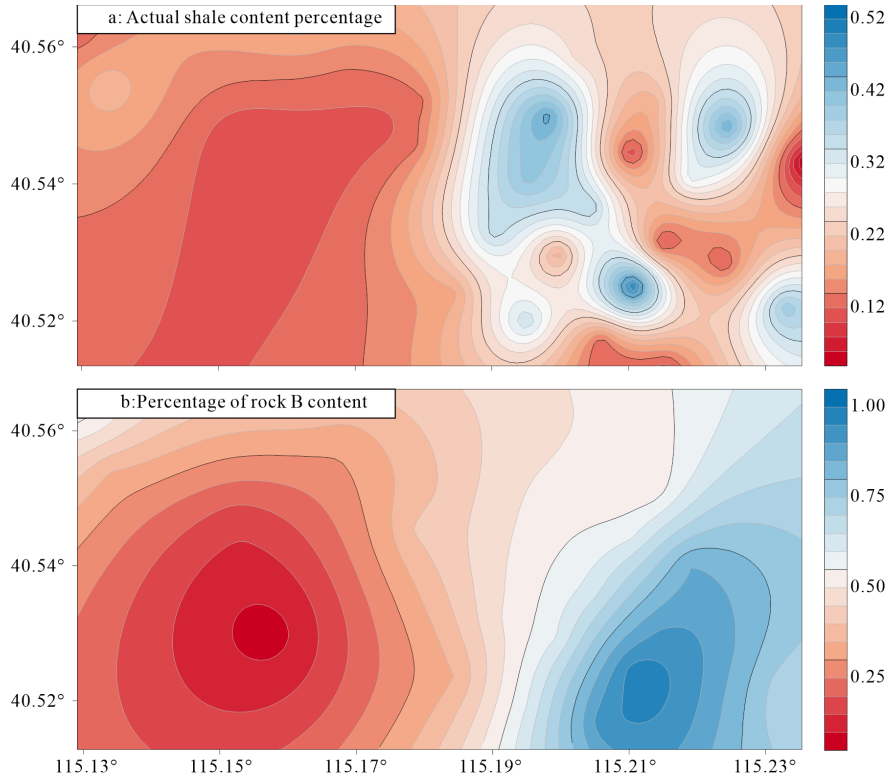


Figure 15. Shale content distribution map (**a**) and rock B percentage prediction (**b**). Based on the comparison images, the trend in large-scale prediction results is consistent. However, due to the current resolution of this method, there is a significant deviation in predicting details.

The presence of developed faults within the area can introduce low-velocity layers that may confound the prediction results. It is important to note that the seismic wave velocity method provides an estimation of rock content based on velocity values, and the actual lithology can be influenced by various geological factors not accounted for in the model. Therefore, the integration of seismic data with drilling data and other geological information is essential for a more accurate assessment of shale gas reservoirs.

Due to the limitations in the precision of this study, it is not possible to further eliminate these influencing factors. In comparison with the predicted results, the content of the shale layers is approximately half of the predicted content of rock B. Thus, a shale content coefficient $k = 0.5$ is introduced for the estimation of the effective shale thickness.

Consequently, the estimation formula for the shale thickness h can be expressed as follows (Formulae (5)):

$$h = k\sum_{i=1}^{n} \Delta H \cdot \frac{V^{-1} - V_A(H_i)^{-1}}{V_B(H_i)^{-1} - V_A(H_i)^{-1}} = k\int_{H_1}^{H_2} \frac{V^{-1} - V_A(H)^{-1}}{V_B(H)^{-1} - V_A(H)^{-1}} dH \quad (5)$$

where ΔH is the thickness corresponding to the layering H_i.

Using this estimation formula, the mudstone shale content from the drilling data was calculated, and the results are presented in Table 1. A correlation test between the predicted shale thickness and the actual shale thickness was conducted [36], yielding a correlation coefficient of 0.58 (Figure 16), indicating a moderate correlation between the predicted and actual values. In the predicted data, 61% of the values deviate by less than 50% from the actual values, and 42% deviate by less than 30%. Therefore, it is considered that the shale thickness predicted by the velocity structure has reference value and can serve as a rapid estimation method for shale in the target layer.

Table 1. Prediction of mudstone shale thickness of the Xiahuayuan Formation.

Well Drilling	Actual Shale Thickness (m)	Predicting Shale Thickness (m)	Well Drilling	Actual Shale Thickness (m)	Predicting Shale Thickness (m)
2–14	171.07	169.69	10–18	302.20	267.38
2–18	323.04	209.80	10–20	205.76	231.43
2–20	223.73	156.56	XD2 3–4	111.11	118.16
2–22	79.12	80.38	X2 1–7	56.44	46.17
4–14	146.05	203.12	X6–16	157.43	216.27
4–16	74.47	221.85	XD2–16	314.31	182.31
4–18	281.44	243.74	X2 11–6	45.10	9.45
4–20	119.52	198.16	X2 13–2	27.04	2.85
4–22	216.79	190.64	X2 39	29.94	71.71
6–14	315.58	256.29	X2 40	28.26	45.42
6–18	55.37	218.99	X2 110	44.70	40.22
6–20	177.50	166.96	X2 116	52.16	50.89
6–22	30.32	111.36	1–6	75.33	104.35
8–14	26.00	244.49	3–1	65.63	99.17
8–18	66.84	238.65	3–2	139.06	142.64
8–22	58.64	240.05			

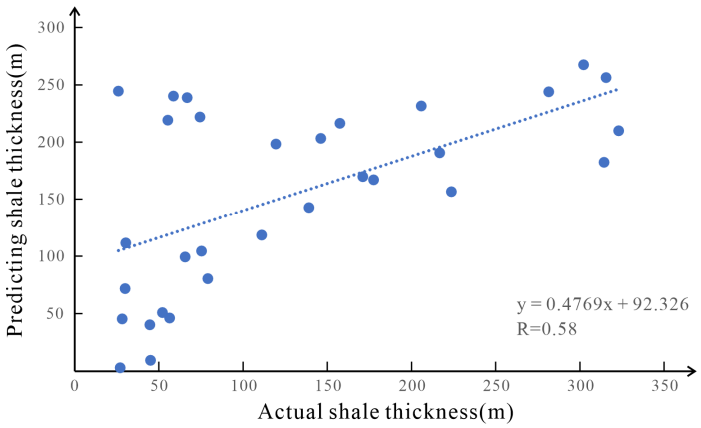


Figure 16. Prediction of mudstone shale thickness with actual mudstone shale thickness.

6. Conclusions

This study utilized a network of 153 nodal seismographs deployed across the shale gas-prone area of Xiahuayuan District in Zhangjiakou to collect 15 days of ambient noise data. Through a comprehensive processing and inversion workflow, a three-dimensional shear wave velocity structure was derived for the depth range of 0–3 km within the prospective shale gas area. The principal conclusions drawn from this research are as follows:

(1) The three-dimensional velocity structure demonstrates sensitivity to variations in velocity values within the 0–3 km depth interval. This sensitivity was confirmed by the sensitivity kernel test, which validated the effectiveness of the model in constraining the subsurface velocity structure. The checkerboard test, employed to reproduce anomalies, revealed that the model can accurately recover anomalies within the 0–3 km depth range, with a horizontal resolution capability of 1.5 km. This affirms the feasibility of applying dense array exploration methods within the shale gas-prone area.

(2) The low-velocity anomalies observed within the velocity structure correlate with the distribution of the Xiahuayuan Formation, likely attributable to the substantial development of shale within this formation. Beneath the Xiahuayuan Formation, within the favorable area, an extensive region of low-velocity structures was identified, which may be indicative of shale presence within the underlying Xiamaling Formation.

(3) A binary model was formulated to predict the shale content using the derived velocity structure. A novel method for estimating the thickness of shale, based on the velocity model, was developed. The predicted outcomes exhibit a moderate correlation with empirical data, suggesting its utility as a rapid estimation technique for assessing the effective shale within the target layer.

(4) The methodologies presented in this study provide an economical and efficient method for the exploration and development of shale gas, with considerable practical application potential.

Author Contributions: Conceptualization, writing—original draft, S.C.; conceptualization, writing—review and editing, Z.L.; writing—review and editing, H.W.; conceptualization, data curation, Q.W.; data curation, W.C.; data curation, G.W. (Guowei Wu); data curation; G.W. (Guangwen Wang). All authors have read and agreed to the published version of the manuscript.

Funding: This study was financially supported by the Tomography of Deep Velocity and Attenuation Structure in the Yin—Wei Basin of the Yellow River Basin, Grant No. Q2401, by the National Natural Science Foundation of China (Grant Nos. 42074115, 42174121 and 91962109), by the National Key Research and Development Program of China, No. 2107YFC0601301, by the Fund from the Key Laboratory of Deep-Earth Dynamics of Ministry of Natural Resources, Grant No. J1901-38, and by the China Geological Survey Project, No. DD20190001.

Data Availability Statement: The relevant data in current research are conserved by Zhanwu Lu. Anyone who wants to use the data can send an email to luzhanwu@cags.ac.cn.

Acknowledgments: Thank you to the Hebei Coalfield Geological Exploration Institute for providing the field geological data. The URLs of the code used in the article are listed below. Thanks to the code author for open-sourcing their work. EGFAnalysisTimeFreq: https://github.com/ShaoboYang-USTC/EGFAnalysisTimeFreq (accessed on 20 October 2024); DSurfTomo: https://github.com/HongjianFang/DSurfTomo (accessed on 20 October 2024).

Conflicts of Interest: The authors declare no conflicts of interest.

References

1. Tian, L.; Wang, Z.; Krupnick, A.; Liu, X. Stimulating shale gas development in China: A comparison with the US experience. *Energy Policy* **2014**, *75*, 109–116. [CrossRef]
2. Zhao, X.; Yang, Y. The current situation of shale gas in Sichuan, China. *Renew. Sustain. Energy Rev.* **2015**, *50*, 653–664.
3. Chen, Y.; Li, J.; Lu, H.; Xia, J. Tradeoffs in water and carbon footprints of shale gas, natural gas, and coal in China. *Fuel* **2020**, *263*, 116778. [CrossRef]
4. Dong, D.; Wang, Y.; Li, X.; Zou, C.; Guan, Q.; Zhang, C.; Huang, J.; Wang, S.; Wang, H.; Liu, H.; et al. Breakthrough and prospect of shale gas exploration and development in China. *Nat. Gas Ind.* **2016**, *36*, 19–32. [CrossRef]
5. Nie, H.; Dang, W.; Zhang, K.; Su, H.; Ding, J.; Li, D.; Liu, X.; Li, P.; Li, P.; Yang, S.; et al. Two decades of shale gas research & development in China: Review and prospects. *Nat. Gas Ind.* **2024**, *44*, 20–52.

6. Zou, C.; Zhai, G.; Zhang, G.; Wang, H.; Zhang, G.; Li, J.; Wang, Z.; Wen, Z.; Ma, F.; Liang, Y.; et al. Formation, distribution, potential and prediction of global conventional and unconventional hydrocarbon resources. *Pet. Explor. Dev.* **2015**, *42*, 13–25. [CrossRef]
7. Liang, X.; Xu, Z.; Zhang, J.; Zhang, Z.; Li, Z.; Jiang, P.; Jiang, L.; Zhu, D.; Liu, C. Key efficient exploration and development technoloiges of shallow shale gas:a case study of Taiyang anticline area of Zhaotong National Shale Gas Demonstration Zone. *Acta Pet. Sin.* **2020**, *41*, 1033–1048.
8. Aki, K. Space and Time Spectra of Stationary Stochastic Waves with Special Reference to Microtremors. *Earthq. Res. Inst.* **1957**, *35*, 415–425.
9. Shapiro, N.M.; Campillo, M.; Stehly, L.; Ritzwoller, M.H. High-Resolution Surface-Wave Tomography from Ambient Seismic Noise. *Science* **2005**, *307*, 1615–1618. [CrossRef]
10. Bensen, G.D.; Ritzwoller, M.H.; Barmin, M.P.; Levshin, A.L.; Lin, F.; Moschetti, M.P.; Shapiro, N.M.; Yang, Y. Processing seismic ambient noise data to obtain reliable broad-band surface wave dispersion measurements. *Geophys. J. Int.* **2007**, *169*, 1239–1260. [CrossRef]
11. Li, J.; Xu, J.; Zhang, H.; Yang, W.; Tan, Y.; Zhang, F.; Meng, L.; Zang, Y.; Miao, S.; Guo, C.; et al. High seismic velocity structures control moderate to strong induced earthquake behaviors by shale gas development. *Commun. Earth Environ.* **2023**, *4*, 188. [CrossRef]
12. Liu, Y.; Zhang, H.; Fang, H.; Yao, H.; Gao, J. Ambient noise tomography of three-dimensional near-surface shear-wave velocity structure around the hydraulic fracturing site using surface microseismic monitoring array. *J. Appl. Geophys.* **2018**, *159*, 209–217. [CrossRef]
13. Wu, Q.; Li, Q.; Hu, X.; Lu, Z.; Li, W.; Wang, X. Ambient noise surface wave tomography of Quaternary structures derived from a high-density array in the central Hebei Depression, North China. *Geosci. J.* **2023**, *27*, 177–190. [CrossRef]
14. Zhang, X.; Lu, Z.; Xiong, X.; Xue, S.; Ren, Y.; Wu, Q.; Wang, G.; Li, Q. Upper crustal structure across the Xiaojiang fault system revealed by ambient noise tomography from a dense short-period array. *Tectonophysics* **2023**, *871*, 230137. [CrossRef]
15. Liu, J.L.; Zhang, J.C.; Li, Z.; Chang, M.H.; Wang, S.; Chen, L.; Yu, H.C. Gas-generation potential of shales in small and medium-sized basins: A case study from the Xuanhua Basin, north China. *Aust. J. Earth Sci.* **2020**, *67*, 411–424. [CrossRef]
16. Xu, S.; Ge, J. Sustainable shifting from coal to gas in North China: An analysis of resident satisfaction. *Energy Policy* **2020**, *138*, 111296. [CrossRef]
17. Tao, J.; Zhang, J.; Liu, J.; Liu, Y.; Dang, W.; Yu, H.; Cao, Z.; Wang, S.; Dong, Z. Molecular and Carbon Isotopic Variation during Canister Degassing of Terrestrial Shale: A Case Study from Xiahuayuan Formation in the Xuanhua Basin, North China. *Minerals* **2021**, *11*, 843. [CrossRef]
18. Shi, M.; Yu, B.; Zhang, J.; Huang, H.; Yuan, Y.; Li, B. Evolution of organic pores in marine shales undergoing thermocompression: A simulation experiment using hydrocarbon generation and expulsion. *J. Nat. Gas Sci. Eng.* **2018**, *59*, 406–413. [CrossRef]
19. Xu, L.; Yang, K.; Wei, H.; Liu, L.; Li, X.; Chen, L.; Xu, T.; Wang, X. Diagenetic evolution sequence and pore evolution model of Mesoproterozoic Xiamaling organic-rich shale in Zhangjiakou, Hebei, based on pyrolysis simulation experiments. *Mar. Pet. Geol.* **2021**, *132*, 105233. [CrossRef]
20. Sabra, K.G.; Gerstoft, P.; Roux, P.; Kuperman, W.A.; Fehler, M.C. Extracting time-domain Green's function estimates from ambient seismic noise. *Geophys. Res. Lett.* **2005**, *32*, 106213. [CrossRef]
21. Yao, H.; Xu, G.; Zhu, L.; Xiao, X. Mantle structure from inter-station Rayleigh wave dispersion and its tectonic implication in western China and neighboring regions. *Phys. Earth Planet. Inter.* **2005**, *148*, 39–54. [CrossRef]
22. Yao, H.; Gouédard, P.; Collins, J.A.; McGuire, J.J.; van der Hilst, R.D. Structure of young East Pacific Rise lithosphere from ambient noise correlation analysis of fundamental- and higher-mode Scholte-Rayleigh waves. *C. R. Geosci.* **2011**, *343*, 571–583. [CrossRef]
23. Dziewonski, A.; Bloch, S.; Landisman, M. A technique for the analysis of transient seismic signals. *Bull. Seismol. Soc. Am.* **1969**, *59*, 427–444. [CrossRef]
24. Dou, L.; Yao, H.; Fang, L.; Luo, S.; Song, M.; Yan, X.; Cheng, C. High-resolution crustal velocity structure in the Shanxi rift zone and its tectonic implications. *Sci. China Earth Sci.* **2021**, *64*, 728–743. [CrossRef]
25. Hou, J.; Pan, J.; Li, Y.; Wu, Z.; Yu, G.; Xu, T. Crustal S-wave velocity structure in the western and central North China Craton and its geological significance. *Chin. J. Geophys.* **2023**, *66*, 1960–1975.
26. Fang, H.; Yao, H.; Zhang, H.; Huang, Y.; van der Hilst, R.D. Direct inversion of surface wave dispersion for three-dimensional shallow crustal structure based on ray tracing; methodology and application. *Geophys. J. Int.* **2015**, *201*, 1251–1263. [CrossRef]
27. Yao, H.; Van Der Hilst, R.D.; de Hoop, M.V. Surface-wave array tomography in SE Tibet from ambient seismic noise and two-station analysis; I, Phase velocity maps. *Geophys. J. Int.* **2006**, *166*, 732–744. [CrossRef]
28. Simons, F.J.; van der Hilst, R.D.; Montagner, J.P.; Zielhuis, A. Multimode Rayleigh wave inversion for heterogeneity and azimuthal anisotropy of the Australian upper mantle. *Geophys. J. Int.* **2002**, *151*, 738–754. [CrossRef]
29. Wang, G.; Lu, Z.; Li, W.; Xue, S.; Wang, H.; Cheng, Y.; Chen, S.; Cai, W. Surface wave imaging using deep reflection seismic data: A study on the Cuonadong dome. *Earth Planets Space* **2022**, *74*, 122. [CrossRef]

30. Herrmann, R.B. Computer programs in seismology; an evolving tool for instruction and research. *Seismol. Res. Lett.* **2013**, *84*, 1081–1088. [CrossRef]
31. Zhang, Z.; Yao, H.; Yang, Y. Shear wave velocity structure of the crust and upper mantle in Southeastern Tibet and its geodynamic implications. *Sci. China Earth Sci.* **2020**, *63*, 1278–1293. [CrossRef]
32. An, M. A simple method for determining the spatial resolution of a general inverse problem. *Geophys. J. Int.* **2012**, *191*, 849–864. [CrossRef]
33. Byun, B.S.; Tran, H.V.; Carter, M.D. An analysis of statistical average velocities in a horizontally layered earth. *Geophysics* **1988**, *53*, 1488–1489. [CrossRef]
34. Chen, S.; Gao, R.; Lu, Z.; Zhang, X.; Li, W.; Liang, Y.; Cheng, Y.; Wang, G. Shallow shear wave velocity structure of the Dongshan sag area using surface wave data in a deep reflection profile of the Yuanmou area of Yunnan province, China. *Tectonophysics* **2022**, *843*, 229606. [CrossRef]
35. Davis, T.L. Velocity variations around Leduc Reefs, Alberta. *Geophysics* **1972**, *37*, 584–604. [CrossRef]
36. Mukaka, M.M. Statistics corner: A guide to appropriate use of correlation coefficient in medical research. *Malawi Med. J.* **2012**, *24*, 69–71.

Disclaimer/Publisher's Note: The statements, opinions and data contained in all publications are solely those of the individual author(s) and contributor(s) and not of MDPI and/or the editor(s). MDPI and/or the editor(s) disclaim responsibility for any injury to people or property resulting from any ideas, methods, instructions or products referred to in the content.